*vaccines*

MDPI

*Article*

# Proteomic Analysis of Human Immune Responses to Live-Attenuated Tularemia Vaccine

Yie-Hwa Chang [1,*,†], Duc M. Duong [2,†], Johannes B. Goll [3,†], David C. Wood [1,†], Travis L. Jensen [3], Luming Yin [2], Casey E. Gelber [3], Nicholas T. Seyfried [2], Evan Anderson [4,5], Muktha S. Natrajan [5,6], Nadine Rouphael [5,6], Robert A. Johnson [7], Patrick Sanz [8], Mark J. Mulligan [9] and Daniel F. Hoft [10]

[1] Edward A. Doisy Department of Biochemistry and Molecular Biology, Saint Louis University Medical School, Saint Louis, MO 63104, USA; david.wood@health.slu.edu

[2] Department of Biochemistry, Emory School of Medicine, Atlanta, GA 30322, USA; dduong@emory.edu (D.M.D.); lyin2@emory.edu (L.Y.); nseyfri@emory.edu (N.T.S.)

[3] The Emmes Company, Rockville, MD 20850, USA; jgoll@emmes.com (J.B.G.); tjensen@emmes.com (T.L.J.); cgelber@emmes.com (C.E.G.)

[4] Department of Pediatrics, Emory University School of Medicine and Children's Healthcare of Atlanta, Atlanta, GA, 30322, USA; evanderson@emory.edu

[5] Division of Infectious Diseases, Department of Medicine, Emory University School of Medicine, Atlanta, GA 30322, USA; muktha.natrajan@emory.edu (M.S.N.); nroupha@emory.edu (N.R.)

[6] Emory Vaccine Center, Emory University, Atlanta, GA 30322, USA

[7] Biomedical Advanced Research and Development Authority, U. S. Department of Health and Human Services, Washington, DC 20201, USA; Robert.Johnson@hhs.gov

[8] Division of Microbiology and Infectious Diseases, National Institute of Allergy and Infectious Diseases, National Institutes of Health, Rockville, MD 20892, USA; patrick.sanz@nih.gov

[9] Division of Infectious Diseases and Immunology, Department of Medicine, and New York University (NYU) Langone Vaccine Center, NYU School of Medicine, New York, NY 10016, USA; mark.mulligan@nyulangone.org

[10] Department of Internal Medicine, Saint Louis University Medical School, Saint Louis, MO 63104, USA; Daniel.hoft@health.slu.edu

* Correspondence: yiehwa.chang@health.slu.edu

† These authors contributed equally to this work.

check for updates

**Abstract:** *Francisella tularensis* (*F. tularensis*) is an intracellular pathogen that causes a potentially debilitating febrile illness known as tularemia. *F. tularensis* can be spread by aerosol transmission and cause fatal pneumonic tularemia. If untreated, mortality rates can be as high as 30%. To study the host responses to a live-attenuated tularemia vaccine, peripheral blood mononuclear cell (PBMC) samples were assayed from 10 subjects collected pre- and post-vaccination, using both the 2D-DIGE/MALDI-MS/MS and LC-MS/MS approaches. Protein expression related to antigen processing and presentation, inflammation (PPARγ nuclear receptor), phagocytosis, and gram-negative bacterial infection was enriched at Day 7 and/or Day 14. Protein candidates that could be used to predict human immune responses were identified by evaluating the correlation between proteome changes and humoral and cellular immune responses. Consistent with the proteomics data, parallel transcriptomics data showed that MHC class I and class II-related signals important for protein processing and antigen presentation were up-regulated, further confirming the proteomic results. These findings provide new biological insights that can be built upon in future clinical studies, using live attenuated strains as immunogens, including their potential use as surrogates of protection.

**Keywords:** proteomics; human immune response; tularemia vaccine; 2D-DIGE; LC-MS/MS; antigen processing; inflammation; phagocytosis; biomarkers

## 1. Introduction

*Francisella tularensis* (*F. tularensis)*, a gram-negative coccobacillus, is an intracellular pathogen of humans and animals that causes a potentially debilitating febrile illness known as tularemia [1–3]. *F. tularensis* infection occurs after exposure to infected wildlife species (including rodents, hares and rabbits), or through bites from infected ticks and deer flies, and causes disease of varying severity dependent upon the portal of entry, the infectious dose, and the subspecies (biovar) of the infecting strain [1–4]. Two biovars have been described: type A, *F. tularensis* biovar *tularensis* and type B, *F. tularensis* biovar *holarctica*. The type A *F. tularensis* subspecies is the most infectious biovar (ID$_{50}$ < 10 cfu), which is responsible for most cases of tularemia in North America. If untreated, this subspecies has mortality rates approaching 30% [3–6]. *F. tularensis* can be spread by aerosol transmission to cause fatal pneumonic tularemia and is therefore classified as a Tier 1 select agent of bioterrorism, indicating its status as one of the most likely pathogens to be deliberately used in a bioterrorist attack [7,8]. Japan, the U.S.A., and the U.S.S.R. have previously stockpiled *F. tularensis* as a potential bioweapon. Given the dangers of *F. tularensis* infection, more research on both the vaccination and molecular-level effects of *F. tularensis* on human health is needed [8–10].

The United States Army Medical Research Institute of Infectious Diseases—LVS (USAMRIID-LVS) live-attenuated vaccine has been used under an investigational new drug (IND) application for decades [11]. However, supply is limited and aging. Thus, the U.S. Department of Defense contracted with Dynport Vaccine Company (DVC) to produce new lots of live vaccine strain (LVS) using current good manufacturing practices (cGMP). It is worth noting that the USAMRIID and DVC-LVS are the same vaccine, that is filed under the same IND application. A phase 1 trial of escalating doses of the new DVC-LVS lot (lot 17) administered to 70 subjects concluded that vaccine delivery by scarification was safe, tolerable, and produced superior antibody responses relative to subcutaneous delivery [12,13]. The data from the phase 2 trial directly compared the new DVC-LVS lot (lot 20) to USAMRIID-LVS in 228 subjects defining the kinetics of antibody responses, comparing injection site reactions following scarification, and correlating antibody responses with take [14]. The availability of pre- and post-vaccination samples from this trial offers a unique opportunity to better characterize host immune responses to this live-attenuated vaccine, to improve vaccine development. As a first step towards this goal, PBMC gene expression responses were previously assessed based on microarrays, following vaccination with two tularemia vaccines [14,15].

In this study, the goal was to comprehensively study protein changes that occur in response to Tularemia DVC-LVS vaccination. Proteomics encompasses the large-scale quantification and identification of the entire set of cellular proteins, as well as the characterization of their modifications, functions, and interactions. It is a powerful tool for studying the host responses to infection and immunization. With the advent of mass spectrometry, microcapillary chromatography, and genome-assisted data analysis, the number, speed, and sensitivity of the proteins and post-translational modifications identified in samples has increased significantly [16]. More importantly, the development of two-dimensional difference gel electrophoresis (2D-DIGE) technology significantly improved reproducibility and accuracy in quantifying proteins expressed within two sets of samples [17,18]. However, one limitation of this technology is its relatively low throughput. To overcome this problem, different quantitative LC-MS/MS methods have been developed, with various advantages and disadvantages. They include spectral-counting, stable isotope labeling by amino acids in cell culture (SILAC), iTRAQ, isotope-coded affinity tag (ICAT) and tandem mass tag (TMT), which have allowed for both absolute and relative quantification of proteins in complex samples [19,20]. Protein microarrays have been developed to track the interactions and activities of pre-determined numbers of proteins in parallel [21,22].

To study the host responses post-vaccination with a live-attenuated tularemia vaccine, 2D-DIGE and LC-MS/MS analyses were performed using PBMC cell lysates from 10 subjects collected pre-vaccination (Day 0) and post-vaccination (Days 7 and 14). PBMC samples were assayed by two different laboratories using two different proteomics protocols. RNA-Seq based transcriptomics, metabolomics

and lipidomics experiments on the same cohort and timepoints which are cross-referenced in the discussion section (23 and unpublished data) were also performed. Here, we report the novel findings regarding the activation of PBMC protein expression related to antigen processing and presentation, inflammation (PPARγ receptor), phagocytosis, and gram-negative bacterial infection following DVC-LVS vaccination.

## 2. Materials and Methods

### 2.1. Study Design

The tularemia vaccine clinical trial (ClinicalTrials.gov identifier NCT01150695) was designed as a double-blind, randomized study of a single, undiluted dose of the *F. tularensis* DVC-LVS lot produced by DynPort Vaccine Company via scarification, versus a single, undiluted dose of the USAMRIID-LVS vaccine via scarification (multiple puncture technique) on Day 0 [12–14]. Both vaccines were administered in the ulnar aspect of the volar surface (palm side) of the forearm midway between the wrist and the elbow [12–14]. Blood samples were taken from enrolled subjects at multiple timepoints. This proteomics pilot study included 10 subjects who had agreed to future-use and had available samples from the DVC-LVS vaccine group, with 30 total samples collected from subjects at Days 0 (prior to vaccination), 7, and 14. In one case, 2D-DIGE methodology for all samples and MALDI-QIT-TOF mass spectrometry to identify proteins within differentially abundant (DA) gel spots were sequentially applied. In parallel, a LC-MS/MS approach was carried out on PBMC lysates after trypsin digestion, followed by protein identification and relative abundance calculation using a label-free quantification method to determine differential protein abundance. Samples from the same subjects were also studied by microarrays [15], RNAseq (unpublished data) and metabolomics [23], as well as lipidomics [23], to determine changes in gene expression, lipids, and metabolites (results of these other omic platforms are reported separately).

### 2.2. Protein Spike-in Controls

A spike-in control protein mixture of bovine beta-lactoglobulin (Sigma L-5137), horse myoglobin (Sigma M-9267), and bovine ribonuclease A (Sigma R-6513) was prepared in 8 M urea. Stock solutions of each protein were prepared in Milli-Q grade water, quantified by UV absorbance spectrum, and combined to make 50 mL of 8 M urea solution containing 300 ng/mL of each protein.

### 2.3. Shared Protein Sequence Database and Protein Families

The combined human subset (organism restricted to *Homo sapiens*), defined by both the UniProtKB/Swiss-Prot and UniPro- tKB/TrEMBL Release 2016-03 databases, was used as a reference for proteomics searches. The *CD-HIT* software (Version 4.0 beta, La Jolla, USA) was used to derive protein clusters at a 50% protein sequence identity level (henceforth, 50% CD-HIT protein clusters are referred to as protein families). Prior to proteomic searching, identical protein sequences were collapsed, and the three spike-in control protein sequences were added to the protein sequence database (UniProt Accession P02754: Beta-lactoglobulin (Bovine), UniProt Accession P68082: Myoglobin (Horse), and UniProt Accession P61823: Ribonuclease pancreatic (Bovine)).

### 2.4. LC-MS/MS Proteomics Experiment and Data Processing

One mL of ice-cold PBS was added to each sample and the samples were centrifuged for 10 min at $400\times g$. Afterwards, 1.5 mL of supernatant was removed and discarded. An additional 500 μL of ice-cold PBS was added and the samples were spun again at $1000\times g$ for 10 min. The supernatant was removed, and the pellet was resuspended in 300 μL of urea lysis buffer (8M Urea spiked with 3 protein spike-in controls), including a 3 μL (100× stock) HALT protease and phosphatase inhibitor cocktail (Pierce). The entire mixture was then sonicated (Sonic Dismembrator, Fisher Scientific) 3 times for 5 s, with 15 s intervals of rest at 30% amplitude to disrupt nucleic acids and was subsequently vortexed.

Protein concentration was determined by the bicinchoninic acid (BCA) method, and samples were frozen in aliquots at −80 °C. Protein homogenates (100 μg) were diluted with 50 mM $NH_4HCO_3$ to a final concentration of less than 2M urea and then treated with 1 mM dithiothreitol (DTT) at 25 °C for 30 min, followed by 5 mM iodoacetamide (IAA) at 25 °C for 30 min in the dark. Protein was digested with 1:100 (*w/w*) lysyl endopeptidase (Wako Chemicals USA, Inc.) at 25 °C for 2 h and further digested overnight with 1:50 (*w/w*) sequencing grade trypsin (Promega Corporation) at 25 °C [17]. Resulting peptides were desalted with a Sep-Pak C18 column (Waters) and dried under vacuum.

Dried peptides were resuspended in 100 μL of loading buffer (0.1% formic acid, 0.03% trifluoroacetic acid, 1% acetonitrile). Peptide mixtures (2 μL) were separated on a self-packed C18 (1.9 μm Dr. Maisch, Germany) fused silica column (25 cm × 75 μM internal diameter (ID); New Objective, Woburn, MA) by a Dionex Ultimate 3000 RSLCNano and monitored on a Fusion mass spectrometer (ThermoFisher Scientific, San Jose, CA). Elution was performed over a 140 min gradient, at a rate of 300 nl/min, with buffer B ranging from 3% to 80% (buffer A: 0.1% formic acid in water, buffer B: 0.1% formic in acetonitrile). The mass spectrometer cycle was programmed to collect at the top speed for 3-s cycles. The MS scans (400–1600 *m/z* range, 200,000 AGC, 50 ms maximum ion time) were collected at a resolution of 120,000 at *m/z* 200 in profile mode and the HCD MS/MS spectra (2 *m/z* isolation width, 30% collision energy, 10,000 AGC target, 35 ms maximum ion time) were detected in the ion trap. Dynamic exclusion was set to exclude previous sequenced precursor ions for 20 s within a 10 ppm window. Precursor ions with +1, and +8 or higher charge states were excluded from sequencing. RAW data for samples were analyzed using MaxQuant v1.5.3.30, with Thermo Foundation for RAW file reading capability. The search engine Andromeda, integrated into MaxQuant, was used to build and search a concatenated target-decoy human reference protein database (20,157 target entries plus 245 contaminant proteins from the common Repository of Adventitious Proteins (cRAP) built into MaxQuant). Methionine oxidation (+15.9949 Da), asparagine and glutamine deamidation (+0.9840 Da), and protein N-terminal acetylation (+42.0106 Da) were variable modifications (up to 5 allowed per peptide); cysteine was assigned a fixed carbamidomethyl modification (+57.0215 Da). Only fully tryptic peptides were considered, with up to 2 miscleavages in the database search. A precursor mass tolerance of ±20 ppm was applied prior to mass accuracy calibration and ±4.5 ppm after internal MaxQuant calibration. Cofragmented peptide search was enabled to deconvolute multiplex spectra. The false discovery rate (FDR) for peptide spectral matches, proteins, and site decoy fraction was set to 1 percent. Quantification settings were as follows: re-quantify with a second peak finding attempt after protein identification has completed; match MS1 peaks between runs; a 0.7 min retention time match window was used after an alignment function was found with a 20-min RT search space. Label-free quantification of proteins and normalization was performed using the MaxLFQ algorithm, as implemented in MaxQuant. The quantitation method only considered razor plus unique peptides for protein level quantitation. Protein group signals were filtered to retain groups, for which at least two unique peptides were identified. Zero intensity values were set to missing. The leading protein in a protein group (the protein with the highest number of identified peptides) was used as the representative protein for each group. Information about other proteins in a protein group was retained and integrated when presenting lists of differentially abundant proteins.

## 2.5. 2D-DIGE/MS Proteomics Experiment and Data Processing

PBMC cell pellets were prepared by the controlled thawing of cryopreserved cells in order to maximize viability, which was assessed by trypan blue stain. Cells were counted by hemocytometer and washed twice with PBS buffer, prior to freezing in aliquots of 2 million viable cells per vial. Cell pellets were lysed, proteins precipitated, and total protein quantified using a Pierce 660 nm protein assay. Prior to carrying out DIGE sub-stoichiometric Cy Dye labeling, an equal protein quantity was taken from each lysate to create a pool for normalization of fluorescence intensity for all analytical 2D gels. This pool was labeled with Cy2 dye, and individual samples were labeled with either Cy3 or Cy5 (Lumiprobe, MD), using a dye ratio of 8 pmol per μg protein [17]. The samples were analyzed by 2D

gel electrophoresis using pH 3–11 NL IPG strips (GE Healthcare) and Criterion XT 4–12% SDS-PAGE gels (BioRad Laboratories, CA). Fluorescence imaging was carried out using a Typhoon 9410. Raw data files were cropped and filtered using ImageQuant TL 8.1 and analyzed using DeCyder 6.5, to determine protein spot relative abundance for Days 7 or 14 versus Day 0. Spots corresponding to spiked proteins were identified using MALDI-TOF mass spectrometry. Forty-one 2D-DIGE gel spots were linked to 68 reference sequence database entries (UniProt IDs).

*2.6. Statistical Analysis*

2.6.1. Normalization

Median normalization was performed to account for systematic differences in protein signal distributions, by aligning the medians of the 30 *log*2 protein signal distributions, which involved the following steps:

(1)    for each sample, the median of the *log*2 protein signal distribution was determined.
(2)    the global median of all 30 sample medians calculated in (1) was obtained.
(3)    a sample specific scaling factor was then calculated as the difference (*log*2 scale) between the global median obtained in (2) and the sample-specific median obtained in (1).
(4)    the *log*2 protein signal distribution for each sample was then median normalized by adding the scaling factor (*log*2 scale), determined in (4).

Local regression (LOESS)-based normalization, as implemented in the *affy* R package (Version 1.48.0), was used to correct systematic signal-dependent non-linear bias observed for Cy5, versus Cy3-labeled 2D-DIGE data samples.

2.6.2. Missing Value Imputation and Log Fold Change from Baseline Calculation

Missing observations were imputed using the k-nearest neighbors algorithm implemented in the impute R package (Version 1.44.0). Only proteins/spots with at least 24/30 (80%) non- missing observations were used as input for imputation and downstream analysis. The number of neighbors to be used as part of the imputation step was set to 8. Subject-specific *log*2 protein fold changes from baseline were calculated based on normalized imputed *log*2 signals for each subject and post-vaccination day (Days 7 and 14), by subtracting baseline (Day 0) protein signals from each of the subject's post-vaccination day signals.

2.6.3. Identification of Differentially Abundant Proteins

Proteins that significantly differed in their response from baseline were identified by using a two-sided permutation paired t-test, comparing post-vaccination (Day x) to baseline (Day 0) protein signals (H0:μ(day$_x$ − day0) = 0, H1:μ(day$_x$ − day0) ≠ 0; on the log2 scale). Proteins with an individual *p*-value <0.05 and baseline fold change ≥1.2 were considered significantly differentially abundant (DA) proteins.

### 2.6.4. Pathway Enrichment Analysis

Pathway enrichment analysis was carried out separately for each post-vaccination day, using 5850 known gene sets obtained from the KEGG Pathway (Version 79.0, 07/16/2016) and MSigDB (Version 5.1, 01/19/2016 including MSigDB Reactome Pathways and MSigDB Immunologic Signatures) databases. Prior to pathway enrichment, proteins in the proteomics protein database were mapped to Ensembl Gene IDs (Ensembl release 84, March 2016), using the biomaRt R package (Version 2.26.1), based on their UniProt protein accessions. If a UniProt protein accession mapped to multiple Ensembl Gene IDs, multiple Ensembl Gene IDs were assigned to that protein. Following the mapping step, genes in gene sets without any UniProt protein accession mappings were excluded from the gene set collections. Gene set statistics after filtering are provided in Table S1.

For each of the filtered gene sets, enrichment was evaluated using the goseq R package (Version 1.12.0), using the hypergeometric distribution to assess statistical significance. To adjust for testing multiple gene sets per category type, the Benjamini–Hochberg procedure was applied to each list. Pathways with an FDR ≤0.1 were considered to be significantly enriched. For significantly enriched KEGG pathways, color-coded KEGG pathway maps were generated (KEGG KGML pathway layout information Version 81.0, 01/06/2017). Node background was color-coded by mean log2 fold change from pre-vaccination (red: up-regulated from baseline, green: down-regulated from baseline). For the 2D-DIGE/MS data, the largest mean $\log_2$ fold change was used for UniProt IDs with multiple gel spot IDs. If nodes in the pathway referred to multiple genes, the median log2 fold change was used to set the background color of that node (red: up-regulated from baseline, green: down-regulated from baseline). If one of the genes of a multi-gene node was significantly enriched, the node label and border was color-coded (red: up-regulated, green: down-regulated, blue: conflict if one gene was up but another was down-regulated for the same pathway node).

### 2.6.5. Identification of Protein Responses that Best Predicted Humoral and Cellular Responses

Regularized linear regression models were fit to determine the 2D-DIGE and LC-MS/MS protein $\log_2$ fold change responses that best predicted peak percent activated CD4$^+$ T-cells (CD3$^+$CD4$^+$CD38$^+$HLA$^-$DR$^+$ cells), peak percent activated CD8$^+$ T-cells (CD3$^+$CD8$^+$CD38$^+$HLA$^-$DR$^+$ cells), and peak microagglutination titer, using the glmnet R package (Version 2.0–13). T-cell and microagglutination data was taken from [14]. T-cell variables were encoded as peak percent activated cells across Days 7, 14, and 28, while tularemia-specific microagglutination was encoded as the $\log_2$ of the peak titer across Days 14 and 28. Leave-one-out cross validation was used to determine the optimum regularization parameters $\alpha$ and $\lambda$, that minimized the model mean squared error. Models were considered to fit the data well if they achieved an $R^2$ of at least 0.7. Correlation networks were for selected proteins were constructed using Pearson correlation ($r \geq 0.4$) and visualized using the R igraph package (Version 1.2.2).

### 2.7. Transcriptomics Data

Transcriptomics data from parallel study were used to assess transcriptome-wide gene expression in PBMCs using RNA-Seq for subjects analyzed in this study (GEO Accession GSE149809).

## 3. Results

In this study, PBMC cell lysates from 10 subjects collected at pre-vaccination (Day 0) and post-vaccination (Days 7 and 14) with a live attenuated tularemia vaccine were assayed by two different laboratories. Each laboratory used a different proteomics protocol. On average, 748 gel spots were identified for each 2D-DIGE gel, while 1872 proteins and 1517 protein families were identified in each sample when using LC-MS/MS (Tables S2–S8).

### 3.1. Technical Assessments and Method Comparisons

Using MALDI-TOF based identification, 2D gels were characterized, resulting in 41 DA gel spots linked to 68 UniProt reference sequence database entries, of which 59 were unique. Thirty-five of these were included in the LC-MS/MS imputed analysis dataset. A listing of all gel spot IDs with protein identifications are provided in Table S4. The agreement of protein abundance for the 35 shared proteins, as measured in $log_2$ label-free quantification (LC/MS/MS) and gel spot volume ratios (2D-DIGE), as well as the agreement between $log_2$ fold change from baseline, was evaluated. The mean Pearson correlation between 2D-DIGE $log_2$ spot volume ratios and the LC-MS/MS $log_2$ label-free quantification for these 35 shared proteins was 0.28 (based on 30 samples). The mean Pearson correlation between baseline $log_2$ fold changes was 0.10 (based on 20 samples).

Boxplots that contrast spike-in protein (beta-lactoglobulin (bovine), myoglobin (horse), and ribonuclease pancreatic (bovine)) variability across the 30 samples, within and between proteomics methods, are displayed in Figure S14. In the 2D-DIGE analysis, RNaseA could not confidently be assigned to a spot in the master gel. Thus, only beta-lactoglobulin and myoglobin were summarized for the 2D-DIGE data. For the LC/MS/MS analysis, RNaseA was identified, but at a much lower abundance than either beta-lactoglobulin or myoglobin (Figures S2–S19). For each proteomics experiment, the coefficient of variation (CV) and robust median absolute deviation (MAD) were calculated (see *x*-axis labels in Figure S14). To compare the variability more directly between experiments, $log_2$ mean-centered protein signals were used. For both experiments, the beta-lactoglobulin (bovine) spike-in protein showed higher variability compared to myoglobin (horse). While beta-lactoglobulin (bovine) was similar in variability (as assessed by MAD) between experiments following normalization, differences were more pronounced for myoglobin (horse). This was also observed when contrasting interquartile ranges for mean-centered protein signals between experiments (Figure S14, bottom right). Overall, the MAD was lower for the 2D-DIGE experiment compared to the LC-MS/MS experiment, with an 8% reduction in MAD for bovine beta- lactoglobulin (0.58 vs. 0.63) and a 33% reduction in MAD for horse myoglobin protein (0.35 vs. 0.52) (Tables S22–S25 and Figures S2–S14).

### 3.2. DA Proteins and Enriched Pathways

A permutation paired t-test to identify vaccine-responsive proteins was performed (Tables S5–S8). Overall, the 2D-DIGE experiment yielded 88 gel spot identifications, that showed DA signals at any post-vaccination day (Day 7 or 14) relative to pre-vaccination (Day 0) (Figure S1). Twenty were shared between post-vaccination days. Notably, 60% percent were upregulated from pre-vaccination (Figure 1 and Figures S20–S29). For the LC-MS/MS experiment, 92 proteins were DA compared to pre-vaccination with 10 being shared between post-vaccination days. Moreover, 96% were up regulated from pre-vaccination (Figure 1 and Figures S20–S29). For both experiments, more DA proteins were identified at day 14 compared to day 7. Four of the 35 (11.4%) shared proteins were DA for both methods (Table 1). For these 4 shared DA proteins, LC/MS/MS data tended to have higher fold changes compared to 2D-DIGE for most proteins. The directions of fold changes for all four DA proteins matched between experiments (all were upregulated from pre-vaccination), ranging from 1.3 to 2.2 -fold increase at Days 7 or 14 compared to pre-vaccination (Table 1). These proteins included TPI1, which plays an important role in energy production/glycolysis (source UniProt) and is related to CD8^{+} T cell activation [24,25], as well as 3 antigen presentation-related proteins comprising KIF5B (involved in MHC class II antigen presentation, source UniProt), HSP90AA1 (involved in chaperoning peptide antigens to be loaded onto MHC I molecules, source: KEGG), and CAPZA1 (involved in MHC class II antigen presentation, source UniProt). The strongest fold change following vaccination for both experiments was observed for the HSP90AA1 chaperone at Day 14 (2.2-fold increase for LC-MS/MS data and 2.0-fold increase for 2D-DIGE data) (Table 1).
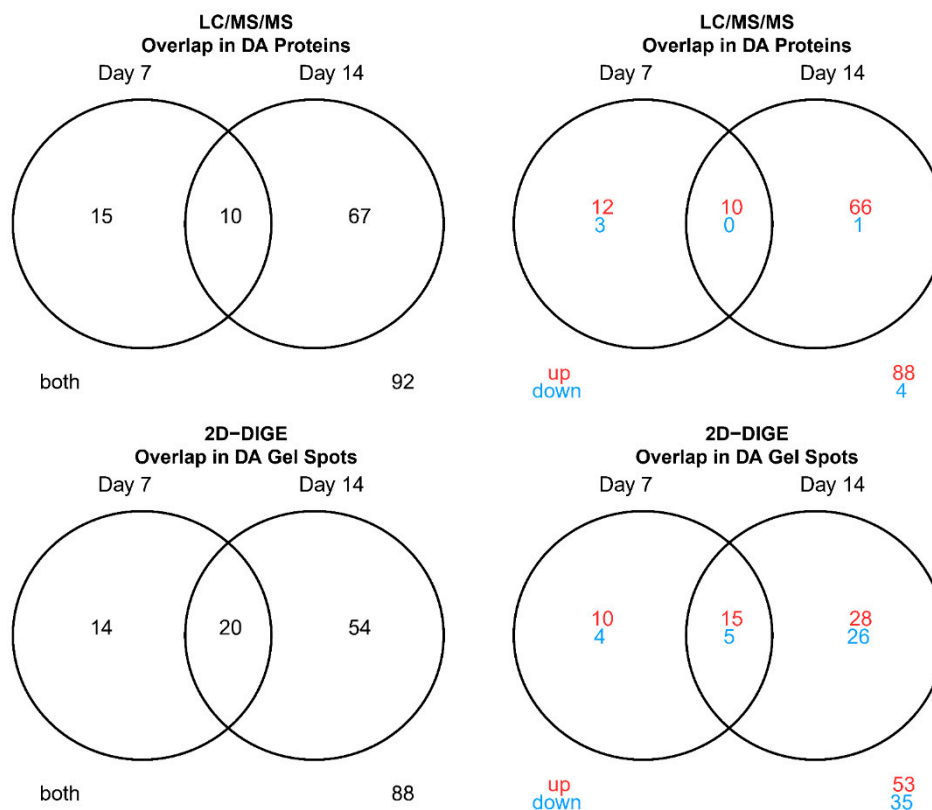
**Figure 1.** Venn diagrams summarizing overlap in differentially abundant (DA) proteins between post-vaccination days (LC-MS/MS and 2D-DIGE/MS). In red: up-regulated compared to pre-vaccination, in green: down- regulated compared to pre-vaccination.

To evaluate the functional context of DA proteins, pathway enrichment analysis was carried out for each experiment (LC-MS/MS and 2D-DIGE/MS data) and post-vaccination day (Days 7 and 14). Significantly enriched KEGG pathways are provided in Table 2. All enrichment results, including those for MSigDB reactome pathways and MSigDB immunologic signatures, are listed in Tables S9–S19. KEGG Pathway enrichment analysis of the 2D-DIGE data showed that the antigen presentation and processing pathway was enriched in DA upregulated proteins on Day 7 and Day 14 (Figure 2). The protein processing in the endoplasmic reticulum pathway was enriched in DA upregulated proteins on Day 14 (Figure 3). Stronger upregulation on Day 14 indicated that there was an increase in antigen presentation response over time. The phagosome pathway was also enriched in DA upregulated proteins on Day 14 (Figure S34). For the LC-MS/MS data, the ribosome pathway was enriched in upregulated DA proteins on both Days 7 and 14, with a stronger enrichment at Day 14 (Figures S30 and S31), while the proteasome pathway was enriched in upregulated DA proteins at Day 14 (Figure 4, Figures S32 and S33). Within the proteasome pathway, the proteins important for the formation of immunoproteasomes, which play a role in preprocessing antigens for presentation on MHC class I molecules, were upregulated (Figure 4, Figures S32 and S33).
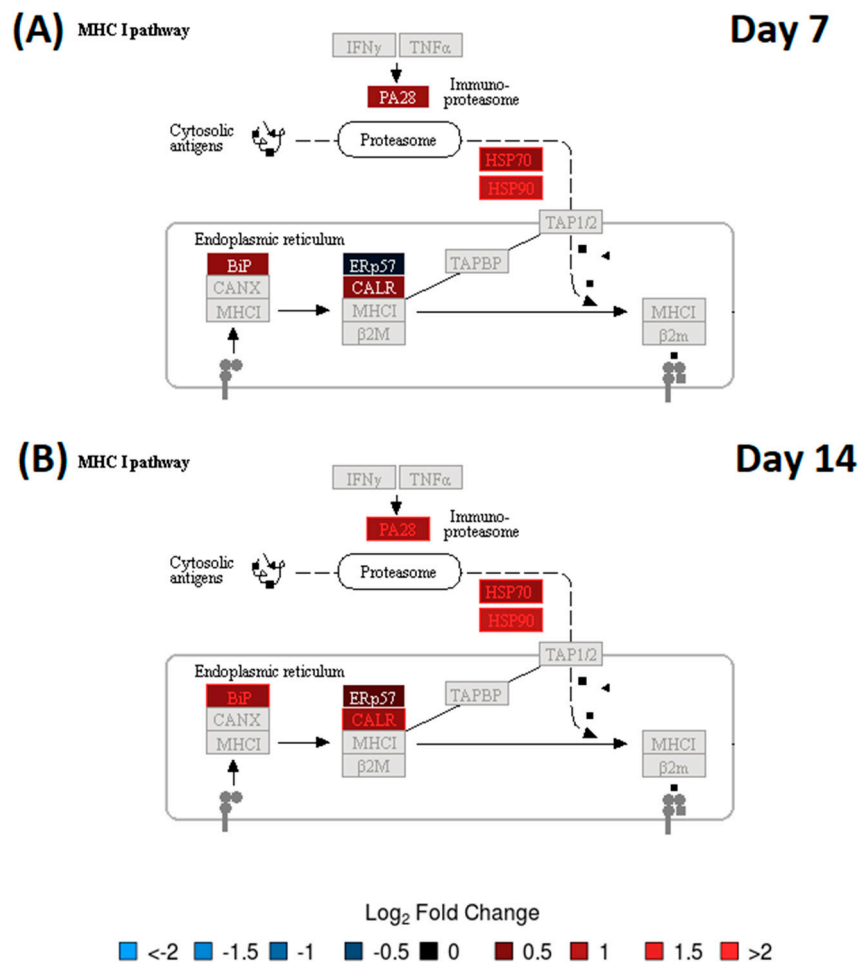
**Figure 2.** KEGG Pathway Map—Antigen processing and presentation (**A**) Day 7 2D-DIGE results (**B**) Day 14 2D-DIGE results. Node color gradient encodes fold change from pre-vaccination (for multi-gene nodes, the median fold change is used). In red: up-regulated compared to Day 0, in blue: down- regulated compared to Day 0, in black: fold change close to 1, in dark grey: proteins were not identified, light grey: gene missing database mapping. Statistically significant fold changes are highlighted using red and blue label colors.

Among immunologic signature gene sets, 5 and 6 signatures were enriched in DA results from LC-MS/MS and 2D-DIGE/MS data, at Day 7 and 14, respectively (Table 3 and Tables S11, S14, S16 and S19). Both *F. tularensis and A. phagocytophilum* are intracellular gram-negative bacteria, which survive and propagate within the host cells. Immunologic signature gene sets related to *A. phagocytophilum* infection were enriched in DA proteins in the data generated from both experiments (Table 3 and Tables S11, S14, S16 and S19). At Day 14, 20 protein families were overlapping for the LC/MS/MS data, with the *A. phagocytophilum* infection set, and 8 protein families were overlapping for the 2D-DIGE dataset (Figures S39–S41 and Table 4 and Tables S10, S13 and S18). These gene sets are based on published human transcriptomic responses in human polymorphonuclear leukocytes following *A. phagocytophilum* infection [26,27]. These latter enrichment results are highly relevant, based on the live-attenuated *F. tularensis* vaccine used for this study.
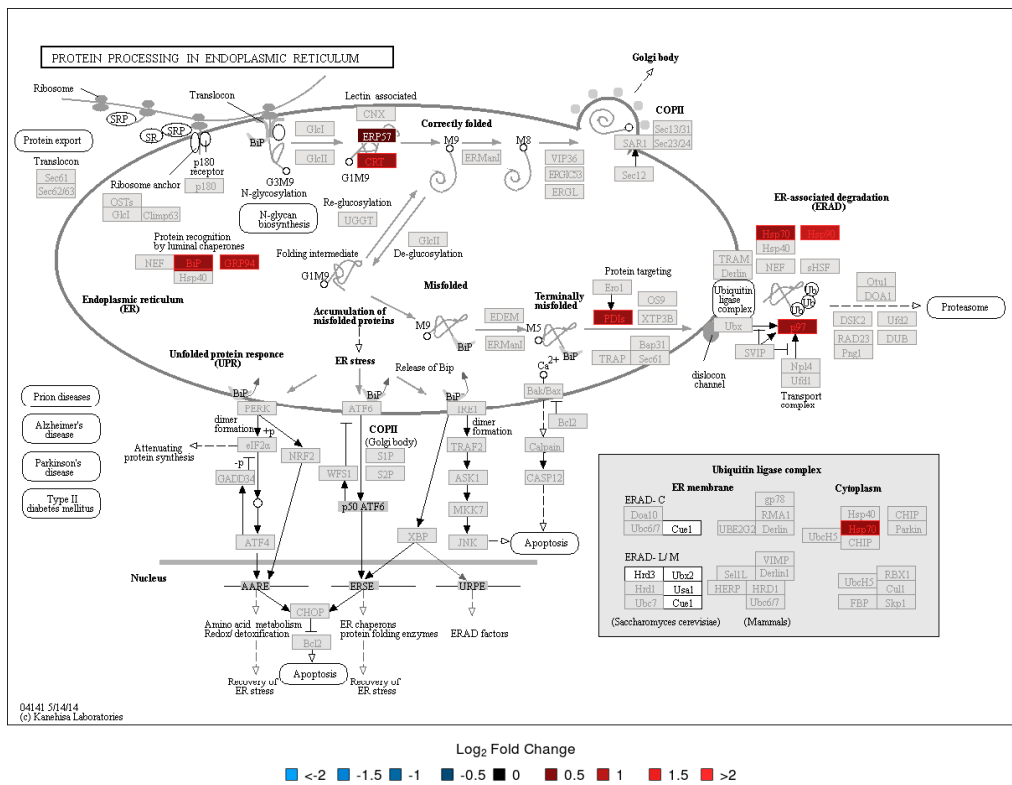
**Figure 3.** KEGG Pathway Map—Protein processing in endoplasmic reticulum Day 14 2D-DIGE/MS results. See Figure 2 caption for interpretation details.
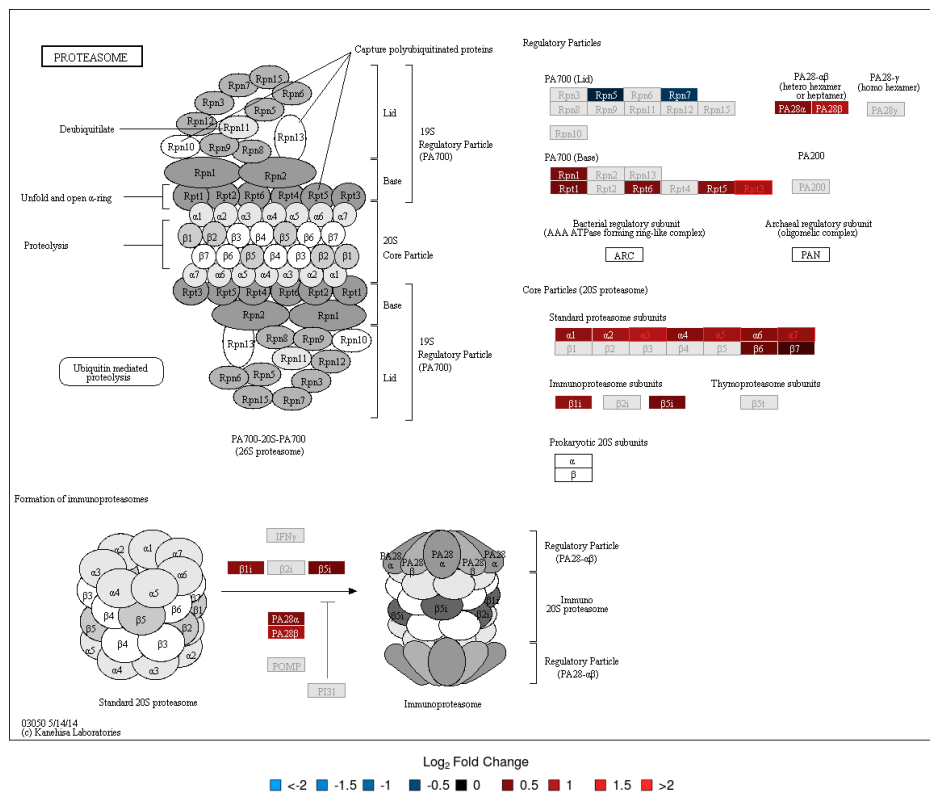


**Figure 4.** KEGG Pathway Map—Proteasome (LC-MS/MS, Day 14). See Figure 3 caption for interpretation details.

**Table 1.** Overlapping differentially abundant proteins (LC-MS/MS and 2D-DIGE/MS). Protein annotations are based on UniProt annotations (March 16, 2016).

| Protein ID | Gene Name | Protein Description | 50% Protein Cluster ID (Gene Name) | LC-MS/MS Time Point | 2D-DIGE/MS Time Point | LC/MS/MS Log$_2$ Fold Change | 2D-DIGE Log$_2$ Fold Change |
|---|---|---|---|---|---|---|---|
| P33176 | KIF5B | Kinesin-1 heavy chain | Q12840 (KIF5A) | Day 7 | Day 7 | 1.11 | 0.33 |
| P33176 | KIF5B | Kinesin-1 heavy chain | Q12840 (KIF5A) | Day 7 | Day 14 | 1.11 | 0.35 |
| P07900 | HSP90AA1 | Heat shock protein HSP 90-alpha | P07900 (HSP90AA1) | Day 14 | Day 7 | 1.12 | 1.00 |
| P60174 | TPI1 | Triosephosphate isomerase | P60174 (TPI1) | Day 14 | Day 7 | 1.12 | 0.58 |
| P07900 | HSP90AA1 | Heat shock protein HSP 90-alpha | P07900 (HSP90AA1) | Day 14 | Day 14 | 1.12 | 1.02 |
| P52907 | CAPZA1 | F-actin-capping protein subunit alpha-1 | P52907 (CAPZA1) | Day 14 | Day 14 | 0.56 | 0.58 |

**Table 2.** Enriched KEGG Pathways (LC-MS/MS and 2D-DIGE/MS). Results within assay and day are sorted by false discovery rate and Jaccard similarity coefficient.

| Assay | Day | Pathway | Pathway Genes # | Significant Genes (%) [Protein Families] | Genes Up (%) | Genes Down (%) | Jaccard Similarity Coefficient | p | FDR-Adjusted P |
|---|---|---|---|---|---|---|---|---|---|
| LC-MS/MS | Day 7 | Ribosome | 127 | 5 (3.9) [5] | 5 (3.9) | 0 (0) | 0.036 | <0.0001 | 0.003 |
| | Day 14 | Ribosome | 127 | 13 (10.2) [14] | 13 (10.2) | 0 (0) | 0.0798 | <0.0001 | <0.0001 |
| | | Proteasome | 44 | 4 (9.1) [4] | 4 (9.1) | 0 (0) | 0.0449 | 0.0003 | 0.0473 |
| 2-DIGE/MS | Day 7 | Pathogenic Escherichia coli infection | 54 | 3 (5.6) [3] | 3 (5.6) | 0 (0) | 0.2273 | 0.0001 | 0.0287 |
| | | Antigen processing and presentation | 64 | 3 (4.7) [2] | 3 (4.7) | 0 (0) | 0.046 | 0.0002 | 0.0287 |
| | | Estrogen signaling pathway | 97 | 3 (3.1) [2] | 3 (3.1) | 0 (0) | 0.0333 | 0.0006 | 0.0653 |
| | Day 14 | Protein processing in endoplasmic reticulum | 159 | 8 (5) [7] | 8 (5) | 0 (0) | 0.0481 | <0.0001 | <0.0001 |
| | | Antigen processing and presentation | 64 | 5 (7.8) [4] | 5 (7.8) | 0 (0) | 0.0745 | <0.0001 | 0.0002 |
| | | Pathogenic Escherichia coli infection | 54 | 4 (7.4) [4] | 4 (7.4) | 0 (0) | 0.2133 | <0.0001 | 0.0023 |
| | | Estrogen signaling pathway | 97 | 4 (4.1) [3] | 4 (4.1) | 0 (0) | 0.0388 | 0.0002 | 0.0175 |
| | | Legionellosis | 48 | 3 (6.2) [2] | 3 (6.2) | 0 (0) | 0.0366 | 0.0005 | 0.0279 |
| | | Phagosome | 142 | 4 (2.8) [4] | 4 (2.8) | 0 (0) | 0.0982 | 0.001 | 0.0498 |

**Table 3.** Overlapping enriched MSigDB Immunologic Signature Sets (LC-MS/MS and 2D-DIGE/MS).

| Category Name | Category Genes | LC-MS/MS | | | 2D-DIGE/MS | | |
|---|---|---|---|---|---|---|---|
| | | Sig. Genes (%) [Protein Fam.] | Jaccard Similarity Coefficient | FDR | Sig. Genes (%) [Protein Fam] | Jaccard Similarity Coefficient | FDR |
| **Day 7** | | | | | | | |
| GSE41978 KLRG1 HIGH VS LOW EFFECTOR CD8 TCELL DN | 186 | 5 (2.7) [5] | 0.0244 | 0.0101 | 3 (1.6) [3] | 0.0234 | 0.0543 |
| GSE41978 ID2 KO VS ID2 KO AND BIM KO KLRG1 LOW EFFECTOR CD8 TCELL DN | 190 | 5 (2.6) [5] | 0.0239 | 0.0101 | 5 (2.6) [5] | 0.0324 | 0.0006 |
| GSE2405 0H VS 9H A PHAGOCYTOPHILUM STIM NEUTROPHIL DN | 192 | 5 (2.6) [5] | 0.0237 | 0.0101 | 5 (2.6) [5] | 0.0321 | 0.0006 |
| GSE3982 EOSINOPHIL VS MAST CELL DN | 186 | 4 (2.2) [4] | 0.0194 | 0.0999 | 3 (1.6) [3] | 0.0186 | 0.0543 |
| GSE2405 0H VS 24H A PHAGOCYTOPHILUM STIM NEUTROPHIL UP | 193 | 4 (2.1) [4] | 0.0188 | 0.0999 | 3 (1.6) [3] | 0.0226 | 0.0543 |
| **Day 14** | | | | | | | |
| GSE2405 0H VS 9H A PHAGOCYTOPHILUM STIM NEUTROPHIL DN | 192 | 20 (10.4) [20] | 0.0813 | <0.0001 | 8 (4.2) [8] | 0.0485 | <0.0001 |
| GSE2405 0H VS 24H A PHAGOCYTOPHILUM STIM NEUTROPHIL UP | 193 | 17 (8.8) [17] | 0.068 | <0.0001 | 4 (2.1) [4] | 0.0302 | 0.029 |
| GSE41978 ID2 KO VS ID2 KO AND BIM KO KLRG1 LOW EFFECTOR CD8 TCELL DN | 190 | 12 (6.3) [12] | 0.0476 | <0.0001 | 5 (2.6) [5] | 0.0306 | 0.0045 |
| GSE22886 NAIVE CD8 TCELL VS DC DN | 187 | 5 (2.7) [5] | 0.0195 | 0.0598 | 4 (2.1) [4] | 0.0264 | 0.029 |
| GSE29618 BCELL VS MDC DAY7 FLU VACCINE DN | 191 | 5 (2.6) [5] | 0.0192 | 0.0598 | 5 (2.6) [5] | 0.0304 | 0.0045 |
| GSE23114 PERITONEAL CAVITY B1A BCELL VS SPLEEN BCELL DN | 194 | 5 (2.6) [5] | 0.019 | 0.0601 | 4 (2.1) [4] | 0.0213 | 0.029 |

**Table 4.** Proteins overlapping with enriched *A. phagocytophilum* infection and PPARγ receptor MSigDB Immunologic Signature Sets. (LC-MS/MS and 2D-DIGE/MS, Day 14).

| | GSE2405_0H_VS_24H_A_PHAGOCYTOPHILUM_STIM_NEUTROPHIL_UP | | |
|---|---|---|---|
| **Assay** | **Gene** | **UniProt ID** | **Day 14 Fold Change** |
| 2D DIGE/MS | ACTB;ACTG1 | P60709 | 2.271;2.004 |
| | TUBA1A;TUBA1B;TUBA1C;TUBA3D;TUBA3E;TUBA8 | P68363 | 2.046 |
| | HSPA8 | P11142 | 1.629 |
| | HSPA5 | P11021 | 1.522 |
| LC MS/MS | NPM1 | P06748 | 2.02 |
| | TKT | P29401 | 1.784 |
| | RPS21 | P63220 | 1.702 |
| | RPL30 | P62888 | 1.638 |
| | RPL4 | P36578 | 1.602 |
| | RPL5 | P46777 | 1.559 |
| | RPL7 | P18124 | 1.555 |
| | RPL22 | P35268 | 1.526 |
| | RPS29 | P62273 | 1.503 |
| | RPL3 | P39023 | 1.495 |
| | RPL17 | P18621 | 1.449 |
| | EEF1B2 | P24534 | 1.433 |
| | RPS18 | P62269 | 1.428 |
| | RPS27 | P42677 | 1.349 |
| | RPL6 | Q02878 | 1.327 |
| | EIF3I | Q13347 | 1.309 |
| | BRK1 | Q8WUW1 | 1.271 |
| | GSE2405_0H_VS_9H_A_PHAGOCYTOPHILUM_STIM_NEUTROPHIL_DN | | |
| **Assay** | **Gene** | **UniProt ID** | **Day 14 Fold Change** |
| 2D DIGE/MS | ACTB;ACTG1 | P60709 | 2.271;2.004 |
| | TUBA1A;TUBA1B;TUBA1C;TUBA3D;TUBA3E;TUBA8 | P68363 | 2.046 |
| | HSP90AA1;HSP90AB1 | P07900 | 2.036 |
| | TUBB;TUBB2A;TUBB2B;TUBB3;TUBB4A;TUBB4B | P07437 | 1.857 |
| | YWHAZ | P63104 | 1.848 |
| | CAPZB;CEP128;PSME1 | P47756 | 1.674 |
| | HSPA8 | P11142 | 1.629 |
| | VCP | P55072 | 1.498 |
| LC MS/MS | HSP90AA1 | P07900 | 2.183 |
| | NPM1 | P06748 | 2.02 |
| | EIF4A1 | P60842 | 1.838 |
| | TKT | P29401 | 1.784 |
| | HMGB1 | P09429 | 1.75 |
| | RPS21 | P63220 | 1.702 |
| | RPL30 | P62888 | 1.638 |
| | RPL4 | P36578 | 1.602 |
| | RPL5 | P46777 | 1.559 |
| | RPL7 | P18124 | 1.555 |
| | CHTOP | Q9Y3Y2 | 1.539 |
| | RPL22 | P35268 | 1.526 |
| | RPS29 | P62273 | 1.503 |
| | RPL3 | P39023 | 1.495 |
| | RPL17 | P18621 | 1.449 |
| | EEF1B2 | P24534 | 1.433 |
| | RPS18 | P62269 | 1.428 |
| | RPS27 | P42677 | 1.349 |
| | RPL6 | Q02878 | 1.327 |
| | EIF3I | Q13347 | 1.309 |

**Table 4.** *Cont.*

| | GSE25123_WT_VS_PPARG_KO_MACROPHAGE_DN | | |
|---|---|---|---|
| **Assay** | **Gene** | **UniProt ID** | **Day 14 Fold Change** |
| 2D DIGE/MS | ARHGDIB | P52566 | 1.504 |
| LC MS/MS | SYNCRIP | O60506 | 2.136 |
| | SAMHD1 | Q9Y3Z3 | 2.118 |
| | PSMA4 | P25789 | 1.814 |
| | PTBP1 | P26599 | 1.635 |
| | PSMA5 | P28066 | 1.595 |
| | RPL5 | P46777 | 1.559 |
| | RPL7 | P18124 | 1.555 |
| | EEF1B2 | P24534 | 1.433 |
| | SNX3 | O60493 | 1.247 |
| | **GSE37532_TREG_VS_TCONV_CD4_TCELL_FROM_LN_UP** | | |
| 2D DIGE/MS | HSP90B1 | P14625 | 1.636 |
| LC MS/MS | ATIC | P31939 | 2.222 |
| | NOP56 | O00567 | 2.169 |
| | CCT3 | P49368 | 2.018 |
| | HDGF | P51858 | 1.801 |
| | EEF1D | P29692 | 1.578 |
| | NOP58 | Q9Y2X3 | 1.525 |
| | SMAP | O00193 | 1.452 |
| | **GSE37532_TREG_VS_TCONV_PPARG_KO_CD4_TCELL_FROM_LN_DN** | | |
| 2D DIGE/MS | LCP1 | P13796 | 2.293 |
| | CALR | P27797 | 1.558 |
| | HSPA5 | P11021 | 1.522 |
| | P4HB | P07237 | 1.505 |
| | **GSE37532_WT_VS_PPARG_KO_VISCERAL_ADIPOSE_TISSUE_TREG_UP** | | |
| 2D DIGE/MS | YWHAZ | P63104 | 1.848 |
| LC MS/MS | HDGF | P51858 | 1.801 |
| | HMGB2 | P26583 | 1.757 |
| | TCEA1 | P23193 | 1.661 |
| | PPP6C | O00743 | 1.638 |

The peroxisome proliferator-activated receptor gamma (PPARγ) protein is a major player in resolving inflammation. Lipids 5-HETE, OEA and AEA have all been shown to be ligands for the PPARγ. The LC- MS/MS DA results at Day 14 showed enrichment in published PPARγ-related immunologic signature gene sets, including GSE25123 (gene expression signals in macrophage-specific PPARγ knockout mice) [28,29] with 9 overlapping protein families, GSE37532 (gene expression signals in T cells in mice) [30,31] with 7 overlapping protein families, and GSE37532 (gene expression signals in T-cells obtained from visceral adipose tissue in mice) [31,32] with 5 overlapping protein families (Table 4 and Table S14). The Day 14 2D-DIGE DA data also showed an enrichment in PPARγ-related GSE37532 gene set (gene expression signals in T cells from PPARγ knockout mice) [31,33], with 4 overlapping protein families (Table 4 and Table S19).

### 3.3. Identification of Protein Responses that Best Predicted Humoral and Cellular Responses

To assess the relationship between proteome changes and humoral and cellular responses post-vaccination, we utilized CD4$^+$, CD8$^+$cell activation and tularemia-specific microagglutination titer we collected previously [14]. We applied regularized linear regression models and visualized results using correlation networks (Figure 5). At both days, peak CD4$^+$ and tularemia-specific microagglutination titer were correlated with changes in proteins. At Day 7, a change in proteasome subunit alpha type-2 (PSMA2), known to be involved in MHC Class I antigen presentation, was increased from pre-vaccination and was associated with the tularemia-specific microagglutination titer. The same was observed for ribonuclease inhibitor 1 (RNH1), a ribonuclease/angiogenin inhibitor potentially involved in redox homeostasis, which was also increased and correlated with microagglutination titer at both Day 7 and 14 (Figure 5). An increase in spectrin alpha 1 (SPTA1), keratin 1 (KRT1), solute carrier family 4, anion exchanger, member 1 (SLC4A1), proteolytic signal containing nuclear protein (PCNP) and coactosin-like F-actin binding protein (COTL1) was positively associated with peak CD4$^+$ activation (Figure 5).
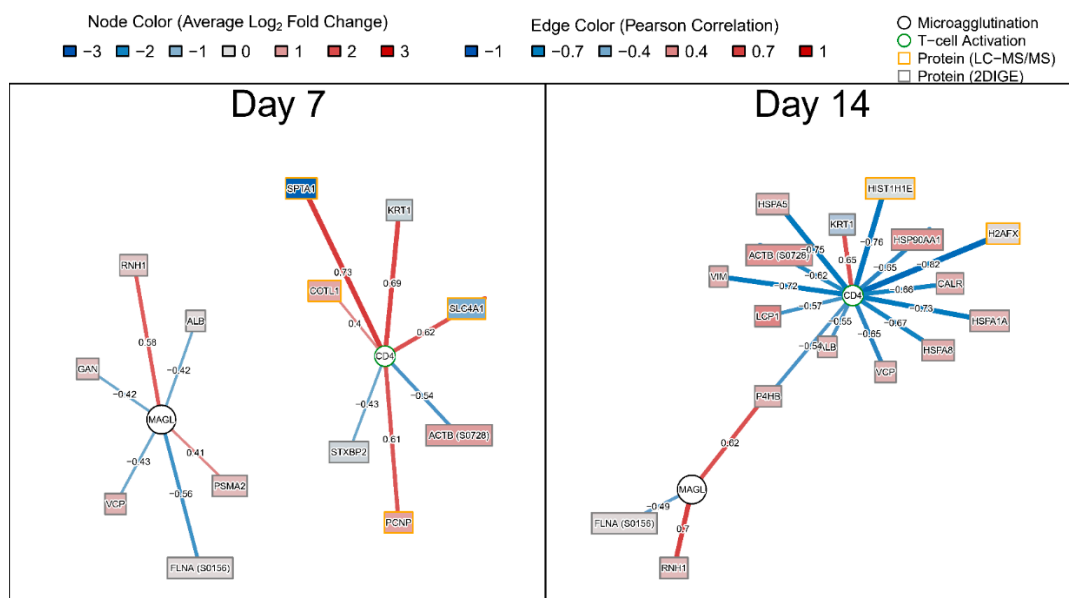


**Figure 5.** Correlation network summarizing associations between changes in proteins and peak cellular and humoral immune responses. Nodes represent protein fold changes (rectangles), peak CD4$^+$ or CD8$^+$ T-cell activation across Days 7, 14, or 28 (green circles), or tularemia-specific peak microagglutination titer across Days 14 and 28 (orange circles). Edges represent the Pearson correlation between log$_2$ protein fold changes and peak CD4$^+$, CD8$^+$ percent T-cell activation, or log$_2$ microagglutination titer. Protein nodes are color-coded by log$_2$ fold change for the respective post-vaccination day. Edges are color coded and edge widths are scaled by Pearson correlation. Nodes were filtered based on Pearson correlation ≥ 0.4 and inclusion as predictors, as part of regularized linear regression models. No correlations were identified for peak CD8$^+$ T-cell activation.

## 4. Discussion

This study expands the efforts to comprehensively characterize immune responses to Tularemia vaccination [14,15,23]. Using both 2-DIGE and LC-MS/MS, changes in proteins in 10 subjects following vaccination were assessed. Three non-human proteins were used as spiked-in controls for both methods for the evaluation of the variability between experiments. Spike-in control protein signals and variability metrics for 3 controls showed that both assays had difficulties with quantifying RNaseA levels. We attribute the lower recovery of RNaseA protein/peptides in the LC/MS/MS analysis to the abundance of cysteine residues and low complexity regions, yielding few proteotypic peptides for sequencing [34]. For the 2-DIGE experiment, we hypothesize that the missing signal of RNaseA was

related to its high isoelectric point value (pI = 9.6). On the other hand, bovine beta-lactoglobulin and horse myoglobin were detected in, on average, 72% and 82% of samples, and showed similar variability for both methods.

The analysis of non-control proteins confirmed that the two different proteomic assays, as expected, produced complementary results [35,36]. This was evident by the small number of shared DA proteins and weak correlation between protein abundance and fold change metrics. In addition, 41% of DA spot proteins identified using MALDI-QIT-TOF were not identified by LC-MS/MS, with a reasonable sample coverage (i.e., ≥80% non-missing values) indicating that missing protein identifications/false negatives play a substantial role. These findings can be explained by multiple factors. First, the proteomics strategies used are technologically very different [36,37]. 2D-DIGE performs analysis on intact proteins, while shotgun LC-MS/MS uses digested peptides. In 2D-DIGE, a mixture of intact proteins is surface labeled with fluorophores, such that the ratio of sample to control fluorescence intensity is proportional to the change in abundance. The labeled proteins are separated by 2-dimensional electrophoresis, which has relatively high resolving power and fluorescence dynamic range but is limited in the total protein applied to the gel, which favors the recovery of high abundance proteins. In LC-MS/MS methods, a chromatographic separation of tryptic peptides is carried out, concurrent with MS/MS sampling of the eluted peptides at high frequency to extract peptide sequence information. These data were analyzed using MaxQuant software to identify proteins in the original lysate and to obtain relative quantifications [37]. These significant differences in the read outs are very likely to affect which proteins are identified from a complex mixture. Thus, it is not surprising that different results in terms of DA protein overlap and abundance and fold change metrics were seen. Second, the preparation of PBMC cell lysates was carried out differently for the two experiments, which may have contributed to the observed differences. Sample preparation methods prior to the lysis of the cells could affect the results, including thawing temperatures, speed of thawing, and cell viability assessments that were not performed for LC- MS/MS analysis. There may be additional differences between the two experiments that are less obvious, and which could affect outcomes. When comparing the data, a higher level of albumin contamination/background was observed in the LC-MS/MS samples. While the 2D-DIGE method separated the albumin out as a single spot (Spot ID: S0522, Table S4), for LC-MS/MS, the resulting albumin peptides were oversampled throughout the gradient. This led to fewer identified peptides and lower quantitative signals for the proteins (peptides) that co-elute. This was evidenced by a strong negative correlation between the abundance of albumin protein and the median protein abundance per sample (Pearson Correlation r = −0.88) in the LC-MS/MS data. This implies that albumin contributed to false negatives and lower fold change accuracy in the LC-MS/MS experiment, by pushing other protein abundances below or near the detection limit. The analysis accounted for this systematic abundance effect using median normalization (scaling up abundances for samples with relatively low medians and scaling down abundances for samples with relatively high medians). However, this median-normalization approach is not designed to correct for missing proteins or the inaccuracy of protein abundances that are pushed close to the detection limit, due to albumin oversampling.

Both proteomic assays indicated that processes related to antigen processing and presentation, and *A. phagocytophilum* infection, were enriched in DA proteins at Day 7 and/or Day 14. The antigen presentation signal at Day 14 showed an increase in the abundance of proteins essential for immunoproteasome formation and an increase in the chaperone protein abundance which is important for MHC class I loading. For the latter, the 2D-DIGE results showed an increasing signal between Days 7 and 14 (both in the number of DA proteins involved in this process as well as in fold change, Figure 3), indicating that MHC class I antigen loading increased during that time. It is known that phagosomes will be formed by antigen presenting cells (APCs) to engulf bacterial pathogens. The phagosomal contents will then be processed after phagolysosomal fusion, and the resulting fragments presented to the antigen specific T lymphocytes in the context of major histocompatibility complex (MHC) surface molecules. Phagocytosis plays a traditional role in providing ligands for MHC-II, but

recent studies suggest that phagosomes might alter the conventional pathway for MHC-II antigen processing in yet undefined ways. MHC-I molecules are normally loaded with peptides derived from cytosolic proteolysis. Although *F. tularensis* shows an extracellular phase during bacteremia in mice, survival and replication within host cells is thought to rely on physical escape from its original phagosome and replication in the host-cell cytosol. As expected, the data revealed that, in addition to the upregulated phagosome pathway, the MHC class I antigen processing and presentation, and proteins related to MHC class II antigen presentation (KIF5B, APZA1) and CD8$^+$ T cell activation (TPI1) were also upregulated post-vaccination. These findings suggest that the LVS is likely to be partially inactivated, and the associated antigens are processed in the phagolysosomes. Processed antigens then enter the MHCI-II antigen presentation pathway, wherein *F. tularensis* antigens surviving in the cytosol of host cells are later processed by the proteasomes for endogenous MHC class I antigen processing.

To further assess these proteomics results in context with the corresponding transcriptomics results based on RNA-Seq (unpublished data), pathway maps were generated that were color-coded by gene expression for KEGG pathways enriched in DA proteins for the complete time course (Days 1,2, 7, and 14) (Figures S42–S73). These results indicated that gene expression within the MHC I sub pathway was significantly up-regulated for PA28 (immunoproteasome subunit), HSP70, and TAP1/2 at Day 2 post-vaccination. These gene expression results returned to near pre-vaccination levels by Day 7. The gene expression of HSP70 remained significantly upregulated from pre-vaccination at Day 7 and Day 14, matching the proteomics results for Day 7 and Day 14. However, in contrast to those proteomic findings, peak levels were observed at Day 2 and increases in gene expression levels for the MHC 1 sub pathway between Days 2 and 14 were not observed. Gene expression signatures related to immunoproteasome formation were up-regulated throughout Days 1–14, but the strongest responses were detected at Day 2 post-vaccination (Figures S46–S49). This indicates that, as expected, peak transcriptomic responses for MHC 1 antigen processing and presentation preceded the corresponding proteomic responses seen at Day 7 (Figures S58–S61) (note, Day 2 samples for proteomics were not tested).

In addition, on the transcriptomics level, there was evidence of an MHC II sub pathway signal, including a significant upregulation of the gene encoding for the MHCII molecule at Day 7 (Figure S60) and the CIITA gene at Day 14 (MHC class II transactivator). While none of the proteins in the MHC II sub pathway showed differential responses at the proteomics level (Figures S35 and S36), the KIF5B and APZA1 proteins that are known to play a role in MHC class II antigen presentation were upregulated in the proteomics experiment at Day 14. Together, these results imply a staggered activation with MHC I presentation to CD8 T cells being activated, first followed by MHC II presentation to CD4 T cells being activated second.

Moreover, both proteomic assays also showed that DA proteins were enriched in PPARγ-related gene sets at day 14 (Tables S14 and S19, Table 4). PPARγ is a ligand-activated transcription factor of the nuclear receptor superfamily, that controls the expression of a variety of genes involved in fatty acid metabolism [38]. Endogenous ligands of PPARγ include fatty acids and eicosanoids [39]. PPARγ can alter macrophage trafficking, and increases efferocytosis and phagocytosis. It also plays a role in the adaptive immune response, particularly regarding B cells [40]. In addition, the activation of PPARγ can shift production from pro- to anti-inflammatory mediators [40]. Interestingly, lipidomic analyses of plasma samples derived from the same subjects revealed increased metabolism (decreased abundance) of the pro-inflammatory 5-hudroxyeicosatetraenoic acid (5-HETE, an eicosanoid) lipid by Day 7 post-vaccination, associated with an apparent compensatory increase in dihydroxyeicosatetraenoic acid (DHET) lipid levels [23]. The pro-inflammatory function of 5-HETE is known to be regulated through conversion to its inactive and less active metabolites, DHET lipids by the Cytochrome P450F family of proteins. Related transcriptomic analyses demonstrated that gene *CYP4F22* was upregulated on Day 2 post-vaccination (1.7-fold increase), Day 7 post-vaccination (1.5-fold increase), and Day 14 post-vaccination (1.8-fold increase). Several Cytochrome P450 family genes, including *CYP1B1* and *CYP4V2*, were also differentially expressed [23]. Because cytochrome P450 genes are important for the

conversion of pro-inflammatory 5-HETE into inactive DHET metabolites, the transcriptomic results further supported the conclusion that 5-HETE is induced early in the acute response to live tularemia vaccination, followed by the induction of Cytochrome P450 gene expression and the subsequent conversion of 5-HETE into inactive DHET species. Consistent with these findings, Muktha et al. found that Tularemia DVC-LVS vaccination induced the production of IFN-gamma detectable in plasma, a signature proinflammatory cytokine, resulting in a statistically significant increase at Day 1 and Day 2 relative to pre-vaccination [15]. Taken together, the data from proteomics, lipidomics and transcriptomics provided interesting new insights into the interplay between Cytochrome P450 family genes, the pro-inflammatory eicosanoid lipids and PPARγ in resolving the Tularemia vaccine induced inflammation.

In addition, at least eight identified proteins were positively associated with peak tularemia-specific microagglutination titer or peak CD4$^+$ activation following vaccination. To our knowledge, this is the first report linking these proteins to human immune responses except for PMSA2 and COTL1. PMSA2 is a subunit of the immunoproteasome which is known to be able to enhance the repertoire of peptides presented by MHC-I molecules [41]. In line with this observation, an increase in PSME1 and PSME2 (Proteasome activator complex subunit 1 and 2) protein following AS03 adjuvanted H5N1 influenza vaccination was observed in monocytes at Day 3, predicting later seroprotection status (based on protective levels of HAI titter) [42]. Furthermore, COTL1, a member of the actin depolymerizing factor (ADF)/cofilin family, is related to the actin-binding protein coactosin, and has been identified as a potential regulator of T cell activation by Kim J. et al. [43] Whether these proteins can be used as novel biomarkers to predict human immune responses remains to be established in larger studies using well established methods, including ELISA, western blot analysis or multiplexed quantitative assays.

## 5. Conclusions

Overall, the analysis confirmed that the two different proteomics assays, as expected, produced complementary results. Some commonalities between the results were identified at the pathway level, including antigen presentation, phagocytosis, inflammation (PPARγ receptor), and gram-negative bacterial infection (*A. phagocytophilum* infection) signals. These results support the biological conclusion that, 14 days following vaccination with a live attenuated tularemia vaccine, abundance for proteins involved in both MHC class I and class II antigen presentation were increased compared to pre-vaccination, including immunoproteasome formation proteins and chaperones for MHC class I loading. In addition, the immunoproteasome subunit protein PMSA2 was associated with tularemia-specific microagglutination titer, linking the MHC class I-related response to the later peak humoral response. Consistent with the proteomics data, our transcriptomic alterations showed that MHC class I and class II-related signals were up-regulated at the gene expression level in a staggered fashion, most likely related to differential timing of transcription first, followed by new protein production, and then increased antigen presentation activity.

The corroborating and complementary data from three 'omics technologies (proteomics, lipidomics, and transcriptomics) provide evidence of how inflammatory response pathways are activated and resolved following live attenuated Tularemia vaccination [15,23]. Although this study was based on a small sample size (10 subjects), the observed DA protein and pathway responses provide new biological insights that can be built upon in future studies, using live attenuated Tularemia strains or other LVS as immunogens, including the assessment of their potential as surrogates of protection.

**Supplementary Materials:** The following are available online at http://www.mdpi.com/2076-393X/8/3/413/s1, Figure S1: Representative 2D-DIGE gel images, Figure S2: Boxplots of proteomics sample metrics (LC-MS/MS), Figure S3: Boxplots of proteomics sample metrics (2D-DIGE/MS), Figure S4: Star plots of proteomics sample metrics (LC-MS/MS), Figure S5: Boxplots of log2 LFQ intensity before median normalization (LC-MS/MS), Figure S6: Boxplots of log2 LFQ intensity after median normalization (LC-MS/MS), Figure S7: Boxplots of log2 spot volume ratios before LOESS normalization (2D-DIGE/MS), Figure S8: Boxplots of log2 spot volume ratios after LOESS normalization (2D-DIGE/MS), Figure S9: ECDF plots of log2 LFQ intensity before and after median normalization (LC-MS/MS), Figure S10: ECDF plots of log2 spot volume ratios before and after LOESS normalization

(2D-DIGE/MS), Figure S11: MA plots of Cy5 versus Cy3 before and after LOESS normalization (2D-DIGE/MS), Figure S12: MA plots of Cy5 versus Cy3 before and after LOESS normalization (2D-DIGE/MS), Figure S13: MA plots of Cy5 versus Cy3 before and after LOESS normalization (2D-DIGE/MS), Figure S14: Boxplots of log2 spike-in control protein signals and variability metrics (LC-MS/MS and 2D-DIGE/MS), Figure S15: ECDF plots of log2 spike-in protein signals (LC-MS/MS and 2D-DIGE/MS, Figure S16: ECDF plots of missing protein observations across samples, Figure S17: Scatterplots of missing observations by average log2 protein signal (LC-MS/MS and 2D-DIGE/MS), Figure S18: PCA and non-metric multidimensional scaling biplots (LC-MS/MS), Figure S19: PCA and non-metric multidimensional scaling biplots (2D-DIGE/MS), Figure S20: Proteomics-based Hierarchical Clustering Plots (LC-MS/MS), Figure S21: Proteomics-based Hierarchical Clustering Plots (2D-DIGE/MS), Figure S22: Venn diagrams summarizing overlap in DA proteins between post-vaccination days (LC-MS/MS and 2D-DIGE/MS), Figure S23: Heatmap of protein log2 fold change from pre-vaccination (LC-MS/MS, Day 7). Rows represent DA proteins, Figure S24: Heatmap of protein log2 fold change from pre-vaccination (LC-MS/MS, Day 14), Figure S25: Heatmap of protein log2 fold change from pre-vaccination (2D-DIGE/MS, Day 7). Rows represent DA proteins, Figure S26: Heatmap of protein log2 fold change from pre-vaccination (2D-DIGE/MS, Day 14). Rows represent DA proteins, Figure S27: Venn diagrams summarizing overlap in DA proteins among 35 proteins with shared identifications for both laboratories (LC-MS/MS and 2D-DIGE/MS), Figure S28: Heatmap of protein log2 fold change for shared DA proteins (LC-MS/MS and 2D-DIGE/MS, Day 7), Figure S29: Heatmap of protein log2 fold change for shared DA proteins (LC-MS/MS and 2D-DIGE/MS, Day 14), Figure S30: KEGG Pathway Map - Ribosome - Homo sapiens (human) (LC-MS/MS, Day 7), Figure S31: KEGG Pathway Map - Ribosome - Homo sapiens (human) (LC-MS/MS, Day 14), Figure S32: KEGG Pathway Map - Proteasome - Homo sapiens (human) (LC-MS/MS, Day 14), Figure S33: KEGG Pathway Map - Protein processing in endoplasmic reticulum - Homo sapiens (human) (2D-DIGE/MS, Day 14), Figure S34: KEGG Pathway Map - Phagosome - Homo sapiens (human) (2D-DIGE/MS, Day 14), Figure S35: KEGG Pathway Map - Antigen processing and presentation - Homo sapiens (human) (2D-DIGE/MS, Day 7), Figure S36: KEGG Pathway Map - Antigen processing and presentation - Homo sapiens (human) (2D-DIGE/MS, Day 14), Figure S37: KEGG Pathway Map - Estrogen signaling pathway - Homo sapiens (human) (2D-DIGE/MS, Day 7), Figure S38: KEGG Pathway Map - Estrogen signaling pathway - Homo sapiens (human) (2D-DIGE/MS, Day 14), Figure S39: KEGG Pathway Map - Pathogenic Escherichia coli infection - Homo sapiens (human) (2D-DIGE/MS, Day 7), Figure S40: KEGG Pathway Map - Pathogenic Escherichia coli infection - Homo sapiens (human) (2D-DIGE/MS, Day 14), Figure S41: KEGG Pathway Map - Legionellosis - Homo sapiens (human) (2D-DIGE/MS, Day 14), Figure S42: KEGG Pathway Map - Ribosome - Homo sapiens (human) (RNA-Seq, Day 1), Figure S43: KEGG Pathway Map - Ribosome - Homo sapiens (human) (RNA-Seq, Day 2), Figure S44: KEGG Pathway Map - Ribosome - Homo sapiens (human) (RNA-Seq, Day 7), Figure S45: KEGG Pathway Map - Ribosome - Homo sapiens (human) (RNA-Seq, Day 14), Figure S46: KEGG Pathway Map - Proteasome - Homo sapiens (human) (RNA-Seq, Day 1), Figure S47: KEGG Pathway Map - Proteasome - Homo sapiens (human) (RNA-Seq, Day 2), Figure S48: KEGG Pathway Map - Proteasome - Homo sapiens (human) (RNA-Seq, Day 7), Figure S49: KEGG Pathway Map - Proteasome - Homo sapiens (human) (RNA-Seq, Day 14), Figure S50: KEGG Pathway Map - Protein processing in endoplasmic reticulum - Homo sapiens (human) (RNA-Seq, Day 1), Figure S51: KEGG Pathway Map - Protein processing in endoplasmic reticulum - Homo sapiens (human) (RNA-Seq,, Day 2), Figure S52: KEGG Pathway Map - Protein processing in endoplasmic reticulum - Homo sapiens (human) (RNA-Seq, Day 7), Figure S53: KEGG Pathway Map - Protein processing in endoplasmic reticulum - Homo sapiens (human) (RNA-Seq, Day 14). Figure S54: KEGG Pathway Map - Phagosome - Homo sapiens (human) (RNA-Seq, Day 1), Figure S55: KEGG Pathway Map - Phagosome - Homo sapiens (human) (RNA-Seq, Day 2), Figure S56: KEGG Pathway Map - Phagosome - Homo sapiens (human) (RNA-Seq, Day 7), Figure S57: KEGG Pathway Map - Phagosome - Homo sapiens (human) (RNA-Seq, Day 14), Figure S58: KEGG Pathway Map - Antigen processing and presentation - Homo sapiens (human) (RNA-Seq, Day 1), Figure S59: KEGG Pathway Map - Antigen processing and presentation - Homo sapiens (human) (RNA-Seq, Day 2), Figure S60: KEGG Pathway Map - Antigen processing and presentation - Homo sapiens (human) (RNA-Seq, Day 7), Figure S61: KEGG Pathway Map - Antigen processing and presentation - Homo sapiens (human) (RNA-Seq, Day 14), Figure S62: KEGG Pathway Map - Estrogen signaling pathway - Homo sapiens (human) (RNA-Seq, Day 1), Figure S63: KEGG Pathway Map - Estrogen signaling pathway - Homo sapiens (human) (RNA-Seq, Day 2), Figure S64: KEGG Pathway Map - Estrogen signaling pathway - Homo sapiens (human) (RNA-Seq, Day 7), Figure S65: KEGG Pathway Map - Estrogen signaling pathway - Homo sapiens (human) (RNA-Seq, Day 14), Figure S66: KEGG Pathway Map - Pathogenic Escherichia coli infection - Homo sapiens (human) (RNA-Seq, Day 1), Figure S67: KEGG Pathway Map - Pathogenic Escherichia coli infection - Homo sapiens (human) (RNA-Seq, Day 2), Figure S68: KEGG Pathway Map - Pathogenic Escherichia coli infection - Homo sapiens (human) (RNA-Seq, Day 7), Figure S69: KEGG Pathway Map - Pathogenic Escherichia coli infection - Homo sapiens (human) (RNA-Seq, Day 14), Figure S70: KEGG Pathway Map - Legionellosis - Homo sapiens (human) (RNA-Seq, Day 1), Figure S71: KEGG Pathway Map - Legionellosis - Homo sapiens (human) (RNA-Seq, Day 2), Figure S72: KEGG Pathway Map - Legionellosis - Homo sapiens (human) (RNA-Seq, Day 7), Figure S73: KEGG Pathway Map - Legionellosis - Homo sapiens (human) (RNA-Seq, Day 14), Table S1: Overview of filtered gene sets used for the gene set enrichment analysis (LC-MS/MS and 2D-DIGE/MS), Table S2: Summary statistics of proteomics sample metrics (LC-MS/MS, *n* = 30), Table S3: Summary statistics of proteomics sample metrics (2D-DIGE/MS, *n* = 30), Table S4: Identified proteins (2D-DIGE/MS). Protein annotations are based on UniProt annotations (March 16, 2016), Table S5: Differentially abundant proteins (LC-MS/MS, Day 7), Table S6: Differentially abundant proteins (LC-MS/MS, Day 14). Sorted by descending absolute log2 fold change, Table S7: Differentially abundant protein gel spots (2D-DIGE/MS, Day 7), Table S8: Differentially abundant protein gel spots (2D-DIGE/MS, Day 14), Table S9: Enriched KEGG Pathways (LC-MS/MS, Day 7), Table S10: Enriched MSigDB Reactome Pathways (LC-MS/MS, Day 7), Table S11: Enriched

MSigDB Immunologic Signature Sets (LC-MS/MS, Day 7), Table S12: Enriched KEGG Pathways (LC-MS/MS, Day 14), Table S13: Enriched MSigDB Reactome Pathways (LC-MS/MS, Day 14), Table S14: Enriched MSigDB Immunologic Signature Sets (LC-MS/MS, Day 14), Table S15: Enriched KEGG Pathways (2D-DIGE/MS, Day 7), Table S16: Enriched MSigDB Immunologic Signature Sets (2D-DIGE/MS, Day 7), Table S17: Enriched KEGG Pathways (2D-DIGE/MS, Day 14), Table S18: Enriched MSigDB Reactome Pathways (2D-DIGE/MS, Day 14), Table S19: Enriched MSigDB Immunologic Signature Sets (2D-DIGE/MS, Day 14). Results are sorted by false discovery rate and Jaccard similarity coefficient, Table S20: Overlapping enriched MSigDB Immunologic Signature Sets (LC-MS/MS and 2D-DIGE/MS, Day 7), Table S21: Overlapping enriched MSigDB Immunologic Signature Sets (LC-MS/MS and 2D-DIGE/MS, Day 14), Table S22: Impact of different normalization procedures on distributions and spike-in metrics (LC-MS/MS), Table S23: Impact of different normalization procedures on distributions and spike-in metrics (2D-DIGE/MS), Table S24: Overlapping differentially abundant proteins (LC-MS/MS and 2D-DIGE/MS), Table S25: List of R packages and versions used for the analyses presented in this report. R version 3.2.5 (2016-04-14).

## References

1. Francis, E. Tularemia. *JAMA* **1983**, *250*, 3216–3224. [CrossRef] [PubMed]

2. McCoy, G.W.; Chapin, C.W. Further observation on a plaguelike disease of rodents with a preliminary note on the causative agent. *J. Infect. Dis.* **1912**, *10*, 61–72. [CrossRef]

3. Francis, E. Deer-fly fever or Pahvant Valley Plague. A disease of man of hitherto unknown etiology. *Public Health Rep.* **1919**, *34*, 2061–2062. [CrossRef]

4. Saslaw, S.; Eigelsbach, H.T.; Wilson, H.E.; Prior, J.A.; Carhart, S. Tularemia vaccine study. I. Intracutaneous challenge. *Arch. Intern. Med.* **1961**, *107*, 689–701. [CrossRef] [PubMed]

5. Saslaw, S.; Eigelsbach, H.T.; Prior, J.A.; Wilson, H.E.; Carhart, S. Tularemia vaccine study. II. Respiratory challenge. *Arch. Intern. Med.* **1961**, *107*, 702–714. [CrossRef]

6. Penn, R.L. Francisella tularensis (tularemia). In *Principles and Practices of Infectious Diseases*, 4th ed.; Mandell, G.L., Douglas, R.G., Bennett, R.G., Bennett, J.E., Eds.; John Wiley and Sons: New York, NY, USA, 2012; pp. 2060–2067.

7. Centers for Disease, C. Outbreak of tick-borne tularemia-South Dakota. *MMWR Rorbid. Mortal. Week Rep.* **1984**, *33*, 601–602.

8. Dennis, D.T.; Inglesby, T.V.; Henderson, D.A.; Bartlett, J.G.; Ascher, M.S.; Eitzen, E.; Fine, A.D.; Friedlander, A.M.; Hauer, J.; Layton, M.; et al. Tularemia as a biological weapon: Medical and public health management. *JAMA* **2001**, *285*, 2763–2773. [CrossRef]

9. Christopher, G.W.; Cieslak, T.J.; Pavlin, J.A.; Eitzen, E.M., Jr. Biological warfare. A historical perspective. *JAMA* **1997**, *278*, 412–417. [CrossRef]

10. Alibek, K.; Handelman, S. *Biohazard: The Chilling True Story of the Largest Covert Biological Weapons Program in the World, Told from the Inside by the Man Who Ran It*; Random House: New York, NY, USA, 1999.

11. Tigertt, W.D. Soviet viable *Pasteurella tularensis* vaccine. A review of selected articles. *Bacteriol. Rev.* **1962**, *26*, 354–373. [CrossRef]

12. Pasetti, M.F.; Cuberos, L.; Horn, T.L.; Shearee, J.D.; Matthews, S.J.; House, R.V.; Sztein, M.B. An improved *Francisella tularensis* Live Vaccine Strain (LVS) is well tolerated and highly immunogenic when administered to rabbits in escalating doses using immunization routes. *Vaccine* **2008**, *26*, 1773–1785. [CrossRef]

13. El Sahly, H.M.; Atmar, R.L.; Patel, S.M.; Wells, J.M.; Cate, T.; Ho, M.; Guo, K.; Pasetti, M.F.; Lewis, D.E.; Sztein, M.B.; et al. Safety, reactogenicity and immunogenicity of *Francisella tularensis* live vaccine strain in humans. *Vaccine* **2009**, *27*, 4905–4911. [CrossRef] [PubMed]

14. Mulligan, M.J.; Stapleton, J.T.; Keitel, W.A.; Frey, S.E.; Chen, W.H.; Rouphael, N.; Edupuganti, S.; Beck, A.; Winokur, P.L.; El Sahly, H.M.; et al. Tularemia vaccine: Safety, reactogenicity, "Take" skin reactions, and antibody responses following vaccination with a new lot of the *Francisella tularensis* live vaccine strain—A phase 2 randomized clinical Trial. *Vaccine* **2017**, *35*, 4730–4737. [CrossRef] [PubMed]

15. Natrajan, M.S.; Rouphael, N.; Lai, L.; Kazmin, D.; Jensen, T.L.; Weiss, D.S.; Ibegbu, C.; Sztein, M.B.; Hooper, W.F.; Hill, H.; et al. Systems vaccinology for a live attenuated tularemia vaccine reveals unique transcriptional signatures that predict humoral and cellular immune responses. *Vacccines* **2020**, *8*, 4. [CrossRef] [PubMed]

16. Gallassie, A.C.; Link, A.J. Proteomics contributions to our understanding of vaccine and immune responses. *Proteom. Clin. Appl.* **2015**, *9*, 972–989. [CrossRef] [PubMed]

17. Unlü, M.; Morgan, M.E.; Minden, J.S. Difference gel electrophoresis: A single gel method for detecting changes in protein extracts. *Electrophoresis* **1997**, *18*, 2071–2077. [CrossRef]

18. Arentz, G.; Weiland, F.; Oehler, M.K.; Hoffmann, P. State of the art of 2D DIGE. *Proteom. Clin. Appl.* **2015**, *9*, 277–288. [CrossRef]

19. Gant-Branum, R.L.; Kerr, T.J.; McLean, J.A. Labeling strategies in mass spectrometry-based protein quantitation. *Analyst* **2009**, *134*, 1525–1529. [CrossRef]

20. Lee, J.R.; Magee, D.M.; Gaster, R.S.; LaBaer, J.; Wang, S.X. Emerging protein array technologies for proteomics. *Expert Rev. Proteom.* **2013**, *10*, 65–75. [CrossRef]

21. Hall, D.A.; Ptacek, J.; Snyder, M. Protein microarray technology. *Mech. Ageing Dev.* **2007**, *128*, 161–167. [CrossRef]

22. Breker, M.; Schuldiner, M. The emergence of proteome-wide technologies: Systematic analysis of proteins comes of age. *Nat. Rev. Mol. Cell Biol.* **2014**, *15*, 453–464. [CrossRef]

23. Maner-Smith, K.M.; Ford, D.A.; Goll, J.B.; Jensen, T.L.; Khadka, M.; Colucci, J.K.; Gelber, C.E.; Albert, C.J.; Bosinger, S.; Franke, J.D.; et al. Alterations in the Human Plasma Lipidome in Response to Tularemia Vaccination. *bioRxiv* **2020**. [CrossRef]

24. Crompton, J.G.; Narayanan, M.; Cuddapah, S.; Roychoudhuri, R.; Ji, Y.; Yang, W.; Patel, S.J.; Sukumar, M.; Palmer, D.C.; Peng, W.; et al. Lineage relationship of CD8$^+$ T cell subsets is revealed by progressive changes in the epigenetic landscape. *Cell. Mol. Immunol.* **2016**, *13*, 502–513. [CrossRef]

25. Pierce, E.L.; Poffenberger, M.C.; Chang, C.H.; Jones, R.G. Fueling immunity: Insights into metabolism and lymphocyte function. *Science* **2013**, *324*, 1242454. [CrossRef] [PubMed]

26. Gene Set: GSE2405_0H_VS_9H_A_PHAGOCYTOPHILUM_STIM_NEUTROPHIL_DN. Available online: http://software.broadinstitute.org/gsea/msigdb/cards/GSE2405_0H_VS_9H_A_PHAGOCYTOPHILUM_STIM_NEUTROPHIL_DN (accessed on 16 March 2016).

27. Borjesson, D.L.; Kobayashi, S.D.; Whitney, A.R.; Voyich, J.M.; Argue, C.M.; Deleo, F.R. Insights into pathogen immune evasion mechanisms: *Anaplasma phagocytophilum* fails to induce an apoptosis differentiation program in human neutrophils. *J. Immunol.* **2005**, *174*, 6364–6372. [CrossRef] [PubMed]

28. Gene Set: GSE25123_WT_VS_PPARG_KO_MACROPHAGE_DN. Available online: http://software.broadinstitute.org/gsea/msigdb/cards/GSE25123_WT_VS_PPARG_KO_MACROPHAGE_DN (accessed on 16 March 2016).

29. Szanto, A.; Balint, B.L.; Nagy, Z.S.; Barta, E.; Dezso, B.; Pap, A.; Szeles, L.; Poliska, S.; Oros, M.; Evans, R.M.; et al. STAT6 transcription factor is a facilitator of the nuclear receptor PPARγ-regulated gene expression in macrophages and dendritic cells. *Immunity* **2010**, *33*, 699–712. [CrossRef]

30. Gene Set: GSE37532_TREG_VS_TCONV_CD4_TCELL_FROM_LN_UP. Available online: http://software.broadinstitute.org/gsea/msigdb/cards/GSE37532_TREG_VS_TCONV_CD4_TCELL_FROM_LN_UP (accessed on 16 March 2016).

31. Cipolletta, D.; Feuerer, M.; Li, A.; Kamei, N.; Lee, J.; Shoelson, S.E.; Benoist, C.; Mathis, D. PPAR-γ is a major driver of the accumulation and phenotype of adipose tissue T reg cells. *Nature* **2012**, *486*, 549–553. [CrossRef]

32. Gene Set: GSE37532_WT_VS_PPARG_KO_VISCERAL_ADIPOSE_TISSUE_TREG_UP. Available online: http://software.broadinstitute.org/gsea/msigdb/cards/GSE37532_WT_VS_PPARG_KO_VISCERAL_ADIPOSE_TISSUE_TREG_UP (accessed on 14 April 2016).

33. Gene Set: GSE37532_TREG_VS_TCONV_PPARG_KO_CD4_TCELL_FROM_LN_DN. Available online: http://software.broadinstitute.org/gsea/msigdb/cards/GSE37532_TREG_VS_TCONV_PPARG_KO_CD4_TCELL_FROM_LN_DN (accessed on 16 July 2016).

34. Kusters, B.; Schirle, M.; Mallick, P.; Aebersold, R. Scoring proteomes with proteotypic peptide probes. *Nat. Rev. Mol. Cell Biol.* **2005**, *6*, 577–583. [CrossRef]

35. Lim, H.; Eng, J.; Yates, J.R., 3rd; Tollaksen, S.L.; Giometti, C.S.; Holden, J.F.; Adams, M.W.W.; Reich, C.I.; Olsen, G.J.; Hays, L.G. Identification of 2D-gel proteins: A comparison of MALDI/TOF peptide mass mapping to µ LC-ESI tandem mass spectrometry. *J. Am. Soc. Mass Spectrum.* **2003**, *14*, 957–970. [CrossRef]

36. Wu, W.W.; Wang, G.; Baek, S.J.; Shen, R.F. Comparative study of three proteomic quantitative methods, DIGE, cICAT, and iTRAQ, using 2D gel-or LC-MALDI TOF/TOF. *J. Proteome Res.* **2006**, *5*, 651–658. [CrossRef]

37. Cox, J.; Mann, M. MaxQuant enables high peptide identification rates, individualized ppb-range mass accuracies and proteome-wide protein quantification. *Nat. Biotechnol.* **2008**, *26*, 1367–1372. [CrossRef]

38. Ament, Z.; West, J.A.; Stanley, E.; Ashmore, T.; Roberts, L.D.; Wright, J.; Nicholls, A.W.; Griffin, J.L. PPAR-pan activation induces hepatic oxidative stress and lipidomic remodeling. *Free Radic. Biol. Med.* **2016**, *95*, 357–368. [CrossRef] [PubMed]

39. Kroker, A.J.; Bruning, J.B. Review of the structure and dynamic mechanisms of PPARγ partial agonism. *PPAR Res.* **2015**, *2015*, 816856. [CrossRef] [PubMed]

40. Croasdell, A.; Duffney, P.F.; Kim, N.; Lacy, S.H.; Sime, P.J.; Phipps, R.P. PPARγ and the innate immune system mediate the resolution of inflammation. *PPAR Res.* **2015**, *2015*, 549691. [CrossRef] [PubMed]

41. Guimarães, G.; Gomes, M.T.R.; Campos, P.C.; Marinho, F.V.; de Assis, N.R.G.; Silveira, T.N.; Oliveira, S.C. Immunoproteasome Subunits Are Required for CD8^{+} T Cell Function and Host Resistance to *Brucella abortus* Infection in Mice. *Infect. Immunity* **2018**, *86*, e00615-17. [CrossRef]

42. Galassie, A.C.; Goll, J.B.; Samir, P.; Jensen, T.L.; Hoek, K.L.; Howard, L.M.; Allos, T.M.; Niu, X.; Gordy, L.E.; Creech, C.B.; et al. Proteomics show antigen presentation processes in human immune cells after AS03-H5N1 vaccination. *Proteomics* **2017**, *17*, 1600453. [CrossRef]

43. Kim, J.; Shapiro, M.J.; Bamidele, A.O.; Gurel, P.; Thapa, P.; Higgs, H.N.; Hedin, K.E.; Shapiro, V.S.; Billadeau, D.D. Coactosin-Like 1 Antagonizes Cofilin to Promote Lamellipodial Protrusion at the Immune Synapse. *PLoS ONE* **2014**, *9*, e85090. [CrossRef]